Nanoscale

PAPER

Check for updates

Tunable single-phase magnetic behavior in chemically synthesized AFeO₃−MFe₂O₄ (A = Bi or La, M = Co or Ni) nanocomposites†

T. Sarkar, [ID] *[a] G. Muscas, [ID] [b] G. Barucca, [ID] [c] F. Locardi, [ID] [d] G. Varvaro,[e] D. Peddis [ID] [e] and R. Mathieu [ID] [a]

The properties of magnetic nanocomposites rely strongly on the interplay between those of the constituent components. When the individual components themselves are complex systems belonging to the family of correlated electron oxide systems which typically exhibit exotic physical properties, it becomes nontrivial to customize the properties of the nanocomposite. In this paper, we demonstrate an easy, but effective method to synthesize and tune the magnetic properties of nanocomposites consisting of correlated electron oxide systems as the individual components. Our method is based on a novel synthesis technique by which the two components of the nanocomposite can be directly integrated with each other, yielding homogeneous samples on the nanoscale with magnetic behavior reminiscent of a single phase. We illustrate our method using multiferroic $BiFeO_3$ (BFO) and $LaFeO_3$ (LFO) as the major phase (*i.e.*, matrix), and MFe_2O_4 (M = Co^{2+} or Ni^{2+}) as the embedded magnetic phase. Furthermore, we show that by a proper selection of the second phase in the nanocomposite, it is possible to customize the magnetic properties of the matrix. We illustrate this by choosing $CoFe_2O_4$ and $NiFe_2O_4$, two oxides with widely differing magnetic anisotropies, as the embedded phase, and demonstrate that the coercivity of BFO and LFO can be increased or decreased depending on the choice of the embedded phase in the nanocomposite.

1. Introduction

Magnetic nanocomposites with tailored properties cover a wide variety of different materials and material combinations[1] that are of huge scientific and technological interest. The wide range of applications of magnetic materials include biomedical applications and catalysis,[2–9] heavy metal removal for wastewater treatment,[10–12] electromagnetic wave absorption and electromagnetic interference shielding,[13–16] in energy devices,[17] and for obtaining improved mechanical[18] and physical[19] properties, such as room temperature giant magnetoresistance.[20] Magnetic nanocomposites consisting of strongly correlated electron oxides[21] as the individual components are particularly interesting owing to their cross-correlated electronic and magnetic properties. They exhibit a multitude of exotic and functional phenomena, such as high-T_c superconductivity,[22] Mott states,[23] spin-liquid states,[24] colossal magnetoresistance,[25] and multiferroicity.[26] The complexity further increases when the particle size is reduced to the nanoscale regime,[27–32] and, furthermore, when two such materials are integrated with each other to form nanocomposites.[33] In such complex systems, the capability to control and tune the properties is extremely important for extending their application in different technological fields. Among those, $BiFeO_3$ (BFO) and $LaFeO_3$ (LFO) are promising perovskite materials exhibiting ferroelasticity and high-temperature antiferromagnetism near 700 K,[34,35] with BFO also being ferroelectric below 1100 K.[35] It is, thus, very relevant to tune and tailor the structural and magnetic properties of these materials in the form of nanocomposites, and bring forth stronger magnetic and/or polar orders and enhanced magnetoelectricity.[36]

In recent years, ferrite-based composites have been increasingly attracting attention due to their diverse applications, and several novel synthesis methods have been reported. For example, core–shell α-Fe_2O_3/$CoFe_2O_4$ composites synthesized using a solvothermal process exhibited enhanced microwave

[a]*Department of Engineering Sciences, Uppsala University, Box 534, SE-75121 Uppsala, Sweden. E-mail: tapati.sarkar@angstrom.uu.se*
[b]*Department of Physics and Astronomy, Uppsala University, Box 516, SE-75120 Uppsala, Sweden*
[c]*Department SIMAU, University Politecnica delle Marche, Via Brecce Bianche, Ancona, 60131, Italy*
[d]*Dipartimento di Chimica e Chimica Industriale, Università degli Studi di Genova, Via Dodecaneso 31, Genova, 16146, Italy*
[e]*Istituto di Struttura della Materia – CNR, Area della Ricerca di Roma1, Monterotondo Scalo, RM, 00015, Italy*
†Electronic supplementary information (ESI) available. See DOI: 10.1039/c8nr06922k
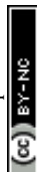
absorption properties.[37] Fe-Based composites derived from Fe_3O_4/Prussian blue composites were synthesized using a controllable carbothermal route, and the magnetic and dielectric properties were studied.[38] Lv et al. reported the synthesis of quaternary $Fe_{0.5}Ni_{0.5}Co_2O_4$ composites via a solvothermal process followed by annealing.[39] FeCo nanoparticles embedded in nanoporous carbon composites were synthesized using a novel method involving thermal conversion of an Fe_3O_4/metal–organic framework.[40] In this paper, we report an easy, low cost, and effective method to synthesize and tune the magnetic properties of nanocomposites where the major phase (i.e., matrix) is composed of a multiferroic material. Conventionally, matrix-based nanocomposites are synthesized by dispersing magnetic nanoparticles in a bulk non-magnetic matrix. Here, we follow a different approach where the matrix itself is nanosized and magnetic (in our case, multiferroic BFO and LFO). The individual matrices of BFO and LFO require different synthesis conditions. Nevertheless, our synthesis method is general, and applicable to several matrices. It is worth noting that BFO and LFO are complex systems, not only in terms of their correlated physical properties, but also as far as their synthesis is concerned. We specifically chose such complex systems owing, not only to their extremely interesting physical properties, but also to prove the robustness of our method, and show that the synthesis technique can be successfully used to prepare complex systems. Both BFO and LFO were synthesized using a modified sol–gel technique, albeit with differences in specific details that are elaborated in section 2.1.2.

To customize the magnetic properties of the nanocomposites, two different spinel ferrites with different anisotropies (i.e., $CoFe_2O_4$ (CFO) and $NiFe_2O_4$ (NFO)) have been chosen as the embedded phase. It is also important to note that our samples are different from epitaxial heterostructures[36] or samples prepared by a templated growth of a magnetic phase in a matrix,[41] where the two component phases are, by design, spatially segregated. The chemical synthesis route that we follow yields samples that are expected to yield a more homogeneous distribution, in the nanoscale, of the embedded phase (CFO or NFO) within the matrix (BFO or LFO) than what is generally achieved using a simple physical mixing of the two phases,[33] the latter often tending to have large clusters of the two phases. This would, in turn, allow for better magnetic coupling between the two phases in our samples, as is indeed evidenced by our magnetic measurements (elaborated in later sections).

In the present study, we present the detailed synthesis, structural, and microstructural characterization, and demonstrate the tunability of the single-phase-like magnetic behavior of the samples.

2. Synthesis and experimental techniques

2.1 Synthesis

2.1.1 $CoFe_2O_4$ and $NiFe_2O_4$.
Cobalt ferrite (CFO) nanoparticles were prepared by a sol–gel self-combustion process.

The details of the self-combustion process and thermogravimetric analysis have been published elsewhere.[42,43] Briefly, 6.7 mmol of $Fe(NO_3)_3 \cdot 9H_2O$ and 3.4 mmol of $Co(NO_3)_2 \cdot 6H_2O$ (Sigma-Aldrich) were mixed in a beaker containing 10 ml of an aqueous solution of 1 M citric acid (1:1 molar ratio of total metals to citric acid). The solution was kept under agitation to dissolve the nitrates at room temperature and NH_3 (30%) was added dropwise to adjust the pH to 7. The solution was heated on a hot plate to 150 °C to form a gel, aided by the chelating action of the citric acid. After approximately 1 h, the entire solution was completely converted to a dry gel, after which the temperature was rapidly increased to 300 °C inducing a flameless self-combustion, which was completed in a few minutes. The final sample was then obtained in the form of a dry powder. Note that no further annealing was required. In order to prepare nickel ferrite nanoparticles (NFO), the same procedure was employed, substituting 3.4 mmol of $Ni(NO_3)_2 \cdot 6H_2O$ in place of the $Co(NO_3)_2 \cdot 6H_2O$ precursor.

2.1.2 $BiFeO_3$ and $LaFeO_3$ matrix.
In a typical synthesis process of BFO, 0.00143 mol of $Bi(NO_3)_3 \cdot 5H_2O$, 0.00143 mol of $Fe(NO_3)_3 \cdot 9H_2O$, and 0.00286 mol of glycine (Sigma-Aldrich) were dissolved in a mixture of 14.3 mL deionized water and 1 mL HNO_3 (65%), under magnetic stirring at ~80 °C. The clear solution was stirred at 80 °C for 20 min. Next, the temperature was increased and maintained at ~150 °C until the formation of a gel. The temperature was then increased to ~250 °C when a self-combustion reaction with a flame occurred, yielding a fluffy powder. The powder was crushed in a mortar, transferred to a furnace, and annealed in air at 350 °C for 1 h, followed by further annealing at 500 °C for an additional 1 h. The sample annealed at 500 °C contained a small amount of Bi_2O_3 impurity that can be removed either by washing with acetic acid or by increasing the annealing temperature to 600 °C.

In a typical synthesis process of LFO, stoichiometric amounts of $La(NO_3)_3 \cdot 6H_2O$ and $Fe(NO_3)_3 \cdot 9H_2O$ were dissolved in deionized water under magnetic stirring at room temperature (ratio of total weight of precursors (in g) : volume of water (in mL) = 1:1). To this solution, ethylene glycol (volume ratio of water : ethylene glycol = 1:1.5) was added. The clear solution was then heated to 80 °C and stirred for 20 min. Next, the temperature was increased and maintained at ~150 °C until the formation of a gel. The temperature was then increased to ~250 °C when a self-combustion reaction with a flame occurred, yielding a fluffy powder. The powder was crushed in a mortar, transferred to a furnace, and annealed in air at 350 °C for 1 h, followed by further annealing at 450 °C for an additional 1 h, and finally at 500 °C for 10 h.

To determine the minimum annealing temperature necessary to obtain a pure phase (that turned out to be 500 °C in our case), the powder obtained after self-combustion was annealed at progressively higher temperatures (in steps of 50 °C i.e., at 350 °C, 400 °C, 450 °C, 500 °C, and so on) and, after each annealing, X-ray diffraction was performed to check the phase purity.

2.1.3 Nanocomposites. The nanocomposites were synthesized by first dispersing an appropriate amount of CFO (or NFO) nanoparticles (synthesized as per the process described in section 2.1.1) in water and sonicating it for ~30 min. Stoichiometric amounts of the respective precursors (of BFO or LFO) were then added, and the exact same steps as described in section 2.1.2 were followed for the synthesis of CFO/BFO (or NFO/BFO) and CFO/LFO (or NFO/LFO) nanocomposites. The amounts of CFO and NFO were chosen such that the weight % of CFO (or NFO) in the nanocomposite corresponded to 2% *i.e.*, CFO (or NFO) : BFO (or LFO) = 2 : 98, by weight. In Fig. 1, we show a flowchart describing the synthesis process of the nanocomposites. A more detailed schematic description of the entire synthesis process is shown in Fig. S1 (in the ESI†).

2.2 Characterization techniques

The samples were characterized by X-ray powder diffraction (XRPD) obtained using a D-5000 diffractometer with CuK_α radiation operating at 40 kV and 30 mA. The data were collected in the range of $2\theta = 20–70°$, with a step size of $0.02°$. The XRPD patterns were also used to estimate the average crystallite size of the samples, using the Williamson–Hall plot.[44]

The composition of the synthesized powders was investigated by energy dispersive spectroscopy (EDS) using a Zeiss SUPRA40 scanning electron microscope (SEM) equipped with a Bruker QUANTAX microanalysis system. Before observations, samples were prepared by spreading some powder on an adhesive conductive carbon disc attached to an SEM aluminium stub.

Inductively coupled plasma optical emission spectroscopy (ICP-OES) was carried out for elemental analysis with an iCAP 6300 DUO ICP-OES spectrometer (ThermoScientific). The samples were digested in *aqua regia* (HCl 37% v/v – HNO_3 69% v/v 3 : 1) for 8 h, then diluted using Milli-Q water, and analysed.

Differential thermal analysis (DTA)/thermogravimetric analysis (TGA) were performed using a LabsysEvo 1600 DTA/TGA (Setaram). 10 mg of sample obtained after self-combustion was put in an alumina crucible and heated from 30 to 1000 °C, at 10 °C min^{-1} under an O_2 atmosphere (20 ml min^{-1}). The DTA and TGA curves were elaborated using the dedicated software Calisto (Setaram).

Transmission electron microscopy (TEM) analysis was performed using a Philips CM200 microscope operating at 200 kV and equipped with a LaB6 filament. For TEM observations, the samples, in the form of powder, were prepared using the following procedure. A small quantity of powder was dispersed in isopropyl alcohol and subjected to ultrasonic agitation for approximately one minute. A drop of suspension was deposited on a commercial TEM grid covered with a thin carbon film; finally, the grid was kept in air until complete evaporation of the isopropyl alcohol.

Temperature and magnetic field-dependent magnetization of the samples was collected using a superconducting quantum interference device (SQUID) magnetometer from
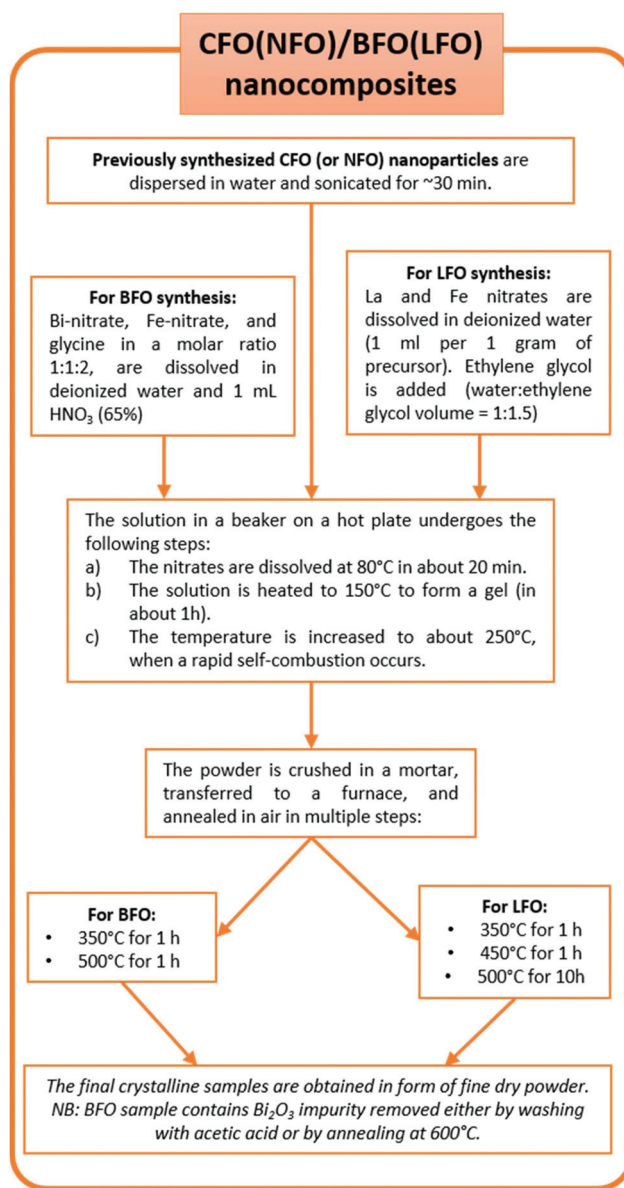

Fig. 1 Flowchart showing the synthesis process of the nanocomposites.

Quantum Design Inc. The temperature dependence of magnetization was recorded under zero-field cooled (ZFC) and field cooled (FC) conditions under a magnetic field $H = 0.05$ T. Magnetic hysteresis loops were recorded at $T = 5$ K in the −5 T to +5 T field range.

3. Results and discussion

3.1 Structural and morphological characterization

The XRPD patterns of the synthesized samples are shown in Fig. 2 and S2 (in the ESI†). The reflections of the cubic CFO (Fig. 2a) and NFO (Fig. 2d) could be indexed to the cubic space group (s.g. $Fd\bar{3}m$). BFO (Fig. 2b) and LFO (Fig. 2e) crystallize in

the rhombohedral (s.g. *R3c*) and orthorhombic (s.g. *Pnma*) structures, respectively. Fig. 2c, 2f, S2a (in the ESI), and S2b (in the ESI†) show the XRPD patterns of the nanocomposites with 2% CFO (or NFO). The CFO and NFO phases either remain undetected in the XRPD patterns (Fig. 2c and S2a†) or only the most intense reflection (311) of the two phases can be observed (Fig. 2f and S2b†). This can be attributed to the extremely low volume % of CFO and NFO in the nanocomposites (~2% in weight). All the observed reflections in the XRPD patterns could be indexed to the expected phases, and no impurity or secondary phase was observed. The average crystallite size (D_{XRPD}) of the samples, as calculated from the XRPD data using the Williamson–Hall plot,[44] varied between 20–25 nm, and have been indicated in the corresponding panels in Fig. 2 and S2 (in the ESI†). The average crystallite size of the samples is also tabulated in Table 1. The estimation of strain from the Williamson–Hall plot shows that the strain does not change appreciably in the nanocomposites as compared to that of the constituent components. The reason for this could be the extremely small amount of the embedded component (only ~2%) in the nanocomposites.

In order to investigate the chemical composition of the synthesized nanoparticles, EDS measurements were performed. The stoichiometry of the as-prepared NFO, CFO, and LFO samples was confirmed by EDS analysis. It is worth mentioning here that the synthesis of BFO was more complicated than the synthesis of LFO because of the presence of an impurity phase of Bi_2O_3 in the as-prepared BFO sample annealed at 500 °C. This impurity phase could be eliminated by a proper choice of the chelating agent, and by performing the final annealing at 600 °C. However, annealing at higher temperature led to an increase in the average crystallite size from ~25 nm

in the sample annealed at 500 °C to ~43 nm in the sample annealed at 600 °C. To avoid such an increase in the crystallite size, we adopted an alternative route to eliminate the Bi_2O_3 impurity phase *i.e.*, by washing the as-prepared sample with acetic acid. However, it is important to remember that we had started the synthesis with stoichiometric proportions of the Bi and Fe precursors, and the presence of a Bi_2O_3 impurity phase might mean that the Bi : Fe ratio in the BFO phase is different from the desired ratio of 1 : 1. Concerning the BFO synthesis, EDS measurements were used to optimize the procedure. It was observed that when ethylene glycol was used as the chelating agent during the synthesis process, the final atomic concentrations of the powder, after washing with acetic acid, exhibited an increase in the Fe content with respect to the Bi content by approximately (5 ± 2)%. This observation can be explained by the formation of the Bi_2O_3 impurity phase, and its subsequent removal by washing with acetic acid (see Fig. S3 in the ESI† for the corresponding XRPD results), leading to the

Table 1 Average crystallite size estimated from XRPD $\langle D_{XRPD} \rangle$, magnetization recorded at 5 T and 5 K ($M_{5\,T}$), and coercive field at 5 K ($H_{C5\,K}$) (errors on the last digit are reported in parenthesis)

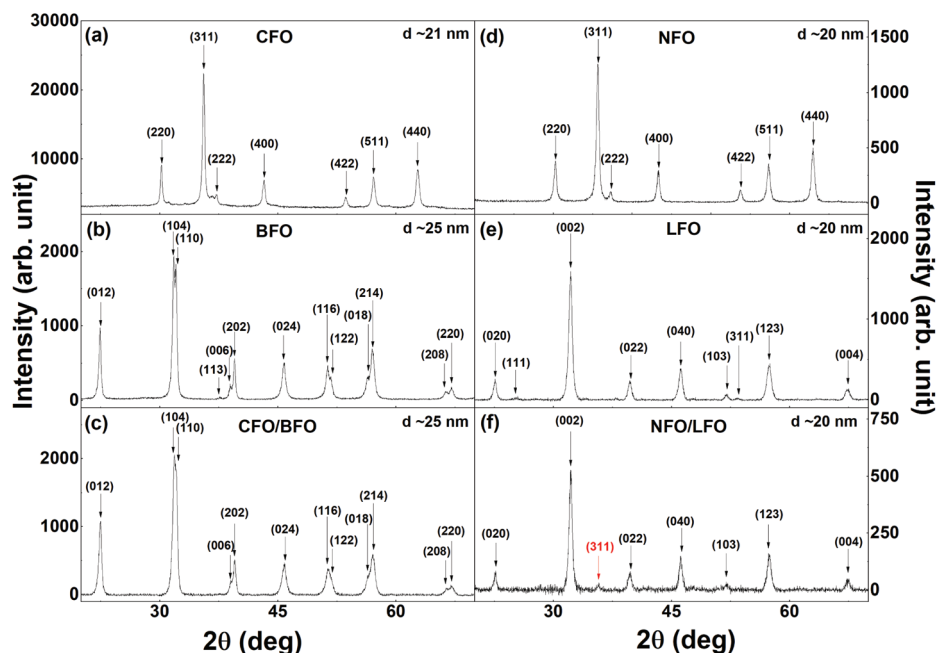| Sample	$\langle D_{XRPD} \rangle$ (nm)	$M_{5\,T}$ (Am² kg⁻¹)	$H_{C5\,K}$ (T)
BFO	25 (2)	1.2 (1)	0.20 (1)
LFO	20 (1)	2.4 (2)	0.08 (1)
CFO	21 (2)	64.0 (1)	1.10 (1)
NFO	20 (1)	40.9 (2)	0.02 (1)
CFO/BFO	25 (2)	2.7 (2)	0.60 (1)
NFO/BFO	25 (2)	2.6 (1)	0.03 (1)
CFO/LFO	20 (2)	7.0 (1)	0.25 (1)
NFO/LFO	20 (2)	5.8 (2)	0.06 (1)

Fig. 2 XRPD patterns of (a) CFO, (b) BFO, (c) CFO/BFO nanocomposites, (d) NFO, (e) LFO, and (f) NFO/LFO nanocomposites.

formation of a non-stoichiometric BFO phase. The amount of Bi_2O_3 in the as-prepared sample could be reduced significantly by using glycine as the chelating agent instead of ethylene glycol (see Fig. S4 in the ESI† for the XRPD patterns). EDS measurements performed on the latter samples (after washing with acetic acid) have confirmed the formation of the stoichiometric BFO phase, even for the sample annealed at 500 °C, thus, indicating that the amount of Bi_2O_3 formed in this sample is small, and does not affect the stoichiometry of the BFO phase appreciably. In order to confirm the weight percent of the spinel ferrite phase in LFO and BFO matrices, ICP analysis was performed on two representative samples, *i.e.*, CFO/BFO and CFO/LFO nanocomposites. Focusing on the Co/Bi and Co/La ratios, weight fractions of 3.1% and 3.9% have been determined for the CFO/BFO and CFO/LFO nanocomposites, respectively. Taking into account the experimental errors, this value can be considered to be in good agreement with the nominal ones. In addition, DTA/TGA (not reported here) has been performed on the LFO/CFO nanocomposite under an O_2 atmosphere. A first weight loss was observed between ~35 and ~210 °C, equal to ~9%, due to some residual solvent and adsorbed moisture. Next, the TG curve showed sequential steps for a total weight loss of ~25% up to 500 °C, and an additional small weight loss (<5%) was observed up to 700 °C. The simultaneously recorded DTA curve revealed a broad exothermic peak in the temperature range of 200–500 °C, suggesting that the weight loss can be ascribed mainly to the combustion of carbonaceous residuals trapped in the composites in some way.[45]

It is worth noting the importance of a proper choice of the chelating agent during synthesis. Different surfactants and chelating agents have been used in sol–gel synthesis, for example, oleic acid,[46,47] polyvinylpyrrolidone,[48] hexamethylenetetramine,[49] ethanolamine,[50] ethyl oleate,[51] and sodium dodecyl benzene sulfonate.[52] In our work, we used different chelating agents to optimize the synthesis. Our experiments revealed that, in the case of CFO and NFO, the use of citric acid enabled phase formation at a temperature as low as 300 °C without the need for any further annealing. In the case of the matrix, ethylene glycol worked well for the synthesis of LFO. However, when we tried to synthesize BFO using ethylene glycol as the chelating agent, a large fraction of Bi_2O_3 was obtained as an impurity phase. The fraction of Bi_2O_3 could be significantly reduced when ethylene glycol was replaced with glycine as the chelating agent.

The morphology of the samples was investigated by transmission electron microscopy; however, due to the low fraction of CFO (and NFO) in the nanocomposites, obtaining information about the morphology and homogeneity of the samples is not trivial. Hence, to facilitate imaging using TEM, we synthesized an additional nanocomposite sample (CFO/LFO) with 10% CFO (see Fig. S2c in the ESI† for the XRPD pattern). Fig. 3a shows a typical bright field TEM image of the sample. The powder is composed of aggregates with size ranging from 200 nm to 3 μm. The agglomerates are made of highly interconnected nanocrystals that give rise to porous

structures (illustrative TEM images are shown in Fig. S5 in the ESI†). Selected area electron diffraction (SAED) measurements performed on numerous agglomerates have revealed the crystalline nature of the sample. Fig. 3b shows a dark field image of the sample shown in Fig. 3a. The image was obtained by selecting diffraction spots corresponding to the $\{121\}_{LFO}$ family planes, and in this way, the LFO nanocrystals responsible for the corresponding diffraction spots are visible. The SAED pattern shown in Fig. 3c was obtained on a portion of the sample shown in Fig. 3a. The major part of the visible diffraction spots is due to the LFO phase and only two spots can be attributed to the CFO phase (white arrows: $\{111\}_{CFO}$ family planes). All the SAED measurements show very few diffraction spots generated by the CFO phase. This result agrees with the small proportion of the CFO phase with respect to the LFO phase (10 : 90 by weight), indicating a very good dispersion of the CFO nanocrystals. Indeed, the presence of clusters of nanocrystals would have generated larger diffraction signals.

One of the CFO nanocrystals is shown in the high-resolution TEM image in Fig. 3d (white outlined area). The distance d among the visible planes, calculated by the fast Fourier transform (FFT) of the image, is 0.484 nm corresponding to the $\{111\}_{CFO}$ interplanar distance.

In order to confirm further the existence and good dispersion of the embedded magnetic phase, a nanocomposite sample (CFO/LFO) with 50% CFO was synthesized. The larger amount of the magnetic phase enabled the TEM analysis to clearly confirm the uniform distribution of CFO and LFO nanocrystals (Fig. S6 in the ESI†). We have also shown typical high resolution TEM images showing the dimensions and structure of few LFO and CFO nanocrystals with the corresponding fast Fourier transforms shown in Fig. S7 and S8 in the ESI.†

3.2 Magnetization measurements

Magnetization *versus* temperature curves of all the synthesized samples were measured in the temperature range of 5–400 K (Fig. S9 and S10 in the ESI†). However, since the ordering temperatures of all the samples lie above 400 K, we were unable to track the variation in the ordering temperatures. Nevertheless, low temperature magnetic field-dependent magnetization measurements were extremely insightful, as elaborated below.

Field dependence of magnetization of the synthesized samples recorded at $T = 5$ K are shown in Fig. 4 and S11 (in the ESI†). We first focus on the curves shown in the left panel of Fig. 4 *i.e.*, the isothermal magnetization curves of CFO (Fig. 4a), BFO (Fig. 4b), and CFO/BFO composites (Fig. 4c). At high magnetic fields ($H = 5$ T), the magnetization of the CFO sample reaches ~64 $Am^2 kg^{-1}$. BFO, on the other hand, is antiferromagnetic, and hence, the magnetization shows no sign of saturation even at high magnetic fields, reaching a value of ~1.2 $Am^2 kg^{-1}$ at $H = 5$ T. The non-zero values of the magnetic remanence and coercivity can be attributed to its weakly ferromagnetic nature arising from finite size effects.[53] Nevertheless,
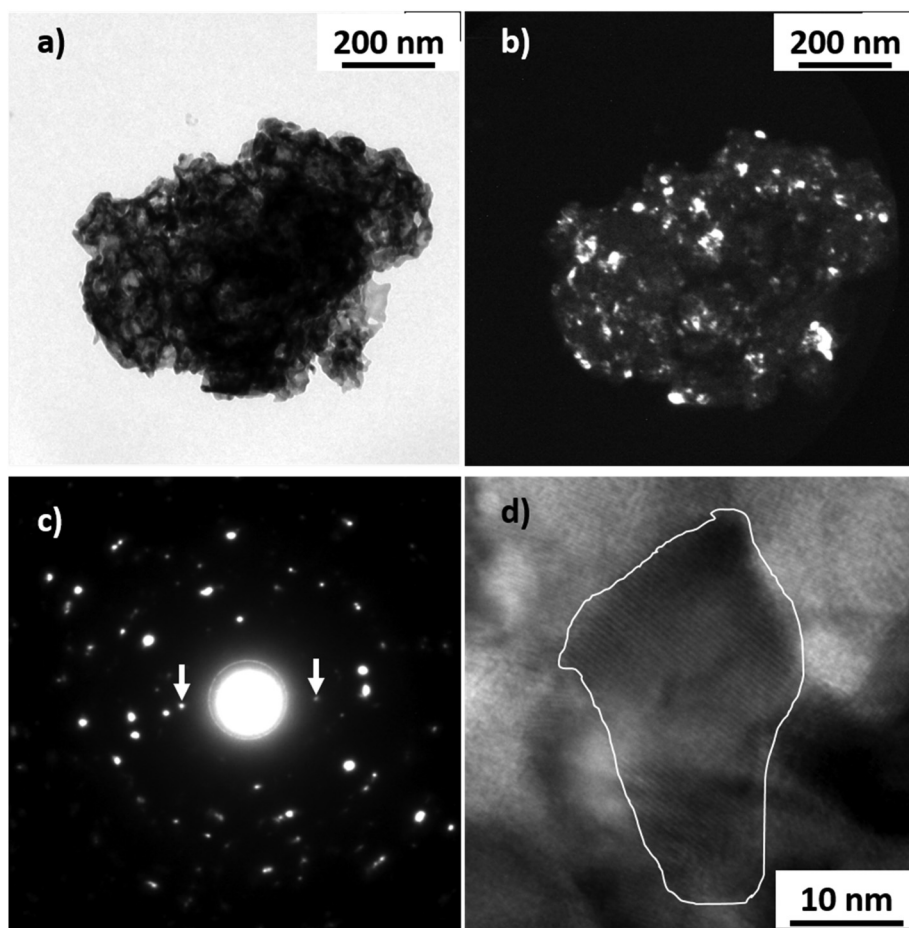
Fig. 3 CFO/LFO (10 : 90 by weight) nanocomposite: (a) TEM bright field image, (b) TEM dark field image showing LFO nanocrystals, (c) corresponding SAED pattern where the {111}$_{CFO}$ diffraction spots are shown by arrows, and (d) high-resolution TEM image of a CFO nanocrystal.

the high field magnetization and coercivity of BFO are considerably smaller than the corresponding values of CFO. Indeed, our experiments revealed that any weight fraction of CFO >2% resulted in the magnetic behavior of the nanocomposite sample being completely dominated by the CFO phase to the extent that the BFO phase was entirely overshadowed (see Fig. S12 in the ESI† for a comparison of the isothermal magnetization curves of pure CFO and CFO/LFO nanocomposites with 10% CFO and 50% CFO).

It is important to note here that despite the presence of two phases in the nanocomposite samples, their magnetic behavior is reminiscent of single phase-like behavior. This is unlike samples prepared *via* simple physical mixing of the two phases, or even some core–shell nanoparticles where anomalous hysteresis behavior has been reported and attributed to the lack of coupling between the two phases.[33,54] In certain cases, the lack of magnetic coupling in physically mixed samples manifests itself in the form of an anomalous hysteretic behavior where the loop shape of the physically mixed sample is close to a simple superposition of the hysteresis loops of the pure individual phases.[33] However, in our case,

the saturation magnetization values of the two individual components (BFO (LFO) and CFO (NFO)) are different by an order of magnitude (Fig. 4). This makes it impossible to see the anomalous hysteretic behavior in the loop shape of the physically mixed samples of BFO (LFO) and CFO (NFO) (not shown here).

A more effective comparison of the magnetic characteristics of the composite *vis-à-vis* that of pure BFO and CFO is possible when we plot the isothermal magnetization curves after normalizing the magnetization axis with respect to the magnetization value at $H = 5$ T, as shown in Fig. 5a. As is evident from the figure, the coercivity of the composite and its normalized remanence (*i.e.* $M_r/M_{5\,T}$) value are intermediates between the corresponding values of BFO and CFO. In other words, we have increased the values of the coercivity and normalized remanence of the composite with respect to that of the BFO matrix.

Next, we investigate what happens when we replace CFO with a ferrite that has a much lower coercivity (*i.e.*, magnetic anisotropy), in this case, NFO. While CFO has a coercivity ($H_{C–CFO}$ ~1.1 T) that is one order larger than that of the BFO
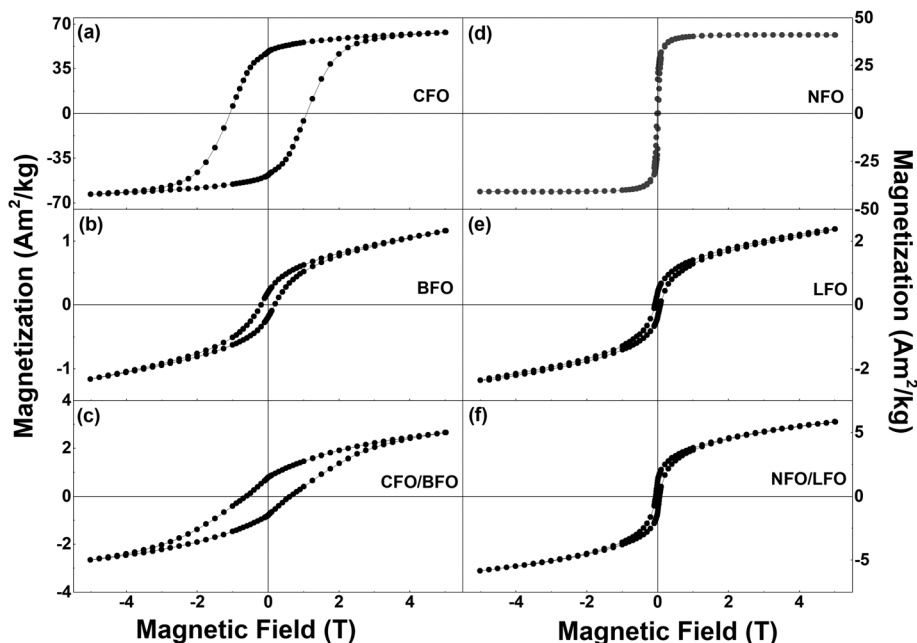
Fig. 4 Isothermal magnetization curves of (a) CFO, (b) BFO, (c) CFO/BFO composite, (d) NFO, (e) LFO, and (f) NFO/LFO composite recorded at $T = 5$ K.
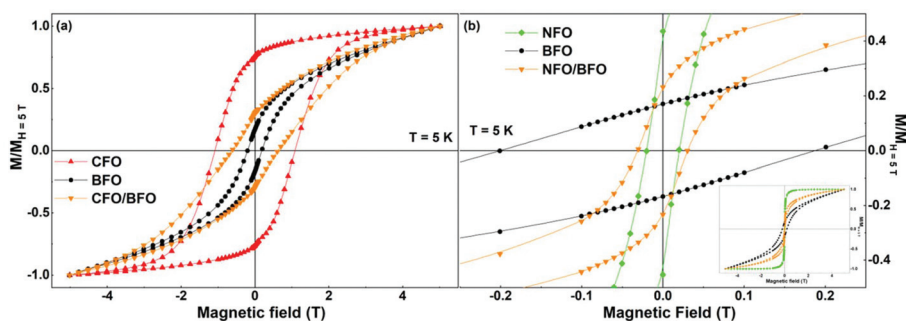

Fig. 5 Normalized isothermal magnetization curves of (a) CFO (red triangles), BFO (black circles), and CFO/BFO composite (orange inverted triangles), and (b) NFO (green diamonds), BFO (black circles), and NFO/BFO composite (orange inverted triangles) recorded at $T = 5$ K (expanded region around the origin). The inset in (b) shows the extended field range from −5 T to +5 T.
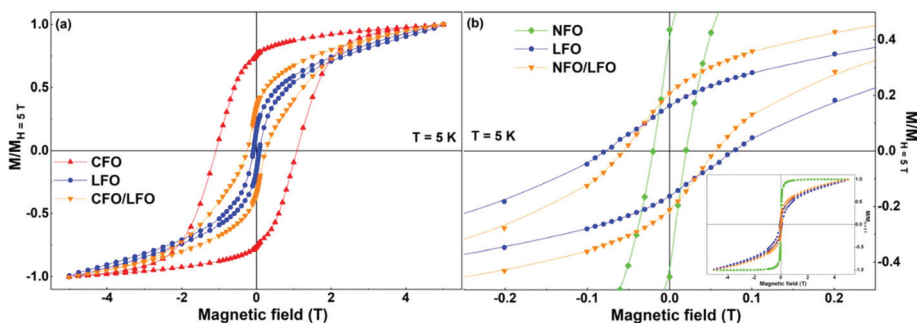

Fig. 6 Normalized isothermal magnetization curves of (a) CFO (red triangles), LFO (blue circles), and CFO/LFO composite (orange inverted triangles), and (b) NFO (green diamonds), LFO (blue circles), and NFO/LFO composite (orange inverted triangles) recorded at $T = 5$ K (expanded region around the origin). The inset in (b) shows the extended field range from −5 T to +5 T.
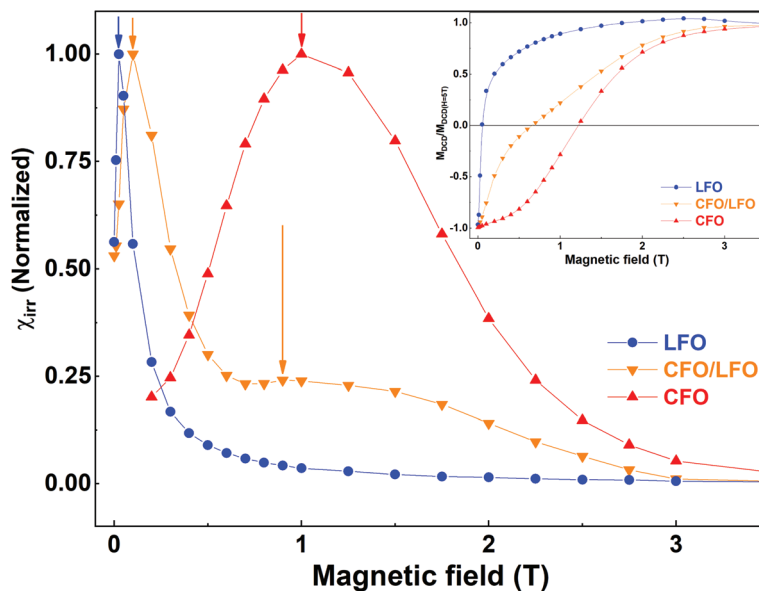
Fig. 7 Inset: Normalized M_{DCD} versus reverse magnetic field of CFO (red triangles), LFO (blue circles), and CFO/LFO composite (orange inverted triangles). Main panel: Corresponding switching field distributions as obtained from the first order derivatives of the M_{DCD} curves.

matrix ($H_{C–BFO}$ ~0.2 T), the coercivity of NFO ($H_{C–NFO}$ ~0.02 T) is one order smaller than that of the BFO matrix. As is clear from Fig. 5b, the NFO/BFO composite also enables us to tune the coercivity of the composite with respect to that of the BFO matrix.

In order to examine whether the aforementioned smooth tuning of the coercivity is specific to the case of BFO, or is a more general trait, we have performed similar experiments with the CFO/LFO and NFO/LFO nanocomposites. The results are illustrated in Fig. 6a and b, where we show the normalized isothermal magnetization curves of LFO, CFO, NFO, and the two composites (CFO/LFO and NFO/LFO). A similar tuning of the coercivity with respect to that of the LFO matrix (increase or decrease depending on whether the composite is synthesized using CFO or NFO nanoparticles) is observed, confirming that our results represent a general feature of composites prepared using the synthesis technique described before.

The magnetic coupling in the nanocomposites can be qualitatively evaluated by remanent magnetization using direct current demagnetization (DCD) experiments.[33,55] The DCD curve is obtained by first saturating the sample in a negative field, and then measuring the magnetization at zero field after applying fields of increasing amplitude. The differentiated curve of M_{DCD} with respect to H represents the irreversible component of susceptibility (χ_{irr}). This quantity can be considered to be a measure of the energy barrier distribution which, in a nanoparticle system, is associated with a particle's switching field distribution (SFD), defined as the field necessary to overcome the energy barrier during an irreversible reversal process.[56] In Fig. 7, we show the measured M_{DCD} curves of LFO, CFO, and CFO/LFO nanocomposites (in the inset), and the corresponding differentiated curves (in the main panel).
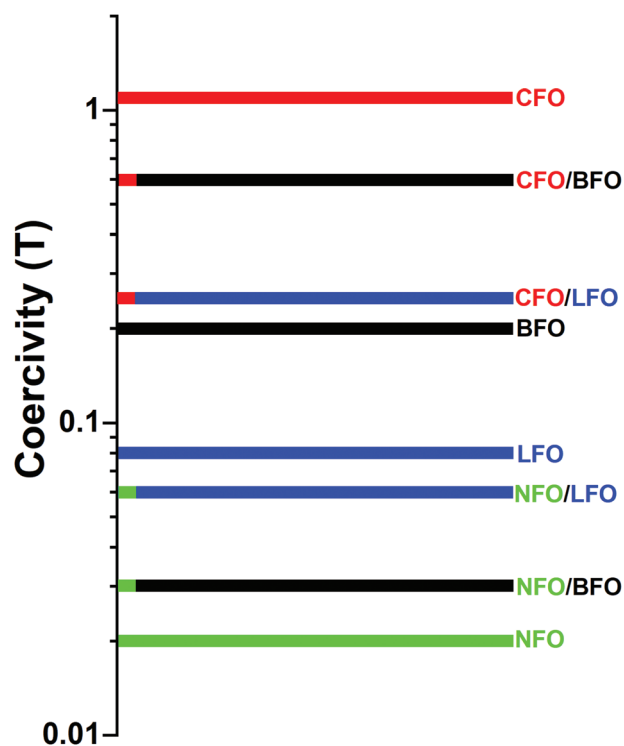

Fig. 8 Schematic representation of the tuning of coercivity by synthesizing nanocomposites. The coercivity values correspond to actual experimental values measured at T = 5 K.

As is clear from the figure, for LFO and CFO, we see strong contributions centered around a single peak (at ~0.03 T for LFO and at ~1.0 T for CFO, indicated by blue and red arrows, respectively). In contrast, in the nanocomposite, the SFD is

centered around two peaks (orange arrows), indicating the individual contributions of the two phases. However, the two peaks do not occur at the same fields as in LFO and CFO. Instead, they are shifted closer with respect to the original pure phases (indicated by the two orange arrows at ~0.1 T and 0.9 T in Fig. 7). This shift indicates the presence of magnetic coupling between the two phases, since the reversal of the two magnetic phases is not independent.[55]

A schematic representation of the coercivity-tuning *via* synthesizing nanocomposites is shown in Fig. 8. Note that the coercivity values in the figure correspond to actual experimental values measured at $T = 5$ K. The magnetic components (CFO and NFO) were chosen such that one had a coercivity much higher than that of the matrix (BFO or LFO) and the other had a coercivity much lower than that of the matrix, so that we could effectively demonstrate the tuning of the coercivity. The tuning of the coercivity due to formation of composites is, in principle, independent of the measuring temperature, and should occur at $T = 300$ K also. However, the phenomenon is not clearly visible from the room temperature *M–H* loops due to the comparable values of coercivity of the individual phases at room temperature. Hence, we have demonstrated this effect using low-temperature *M–H* loops where the effect is clearly visible.

4. Conclusions

In summary, we have synthesized magnetic nanocomposites using CFO or NFO as one component and BFO or LFO as the second component (matrix) *via* a novel chemical synthesis route. Our synthesis route yields superior quality samples with single-phase-like magnetic behavior as compared to samples prepared *via* simple physical mixing of the two phases that have been reported to lack enough coupling between the two phases. Furthermore, we demonstrate a striking tuning of the magnetic coercivity with respect to that of the matrix depending on the choice of the embedded component in the nanocomposites. We believe that these results will be of huge value in the quest for nanocomposites with functional properties.

Conflicts of interest

There are no conflicts of interest to declare.

Acknowledgements

References

1 S. Behrens, Preparation of functional magnetic nanocomposites and hybrid materials: recent progress and future directions, *Nanoscale*, 2011, **3**, 877–892.

2 A. K. Hauser, R. J. Wydra, N. A. Stocke, K. W. Anderson and J. Z. Hilt, Magnetic nanoparticles and nanocomposites for remote controlled therapies, *J. Controlled Release*, 2015, **219**, 76–94.

3 M. B. Gawande, Y. Monga, R. Zboril and R. K. Sharma, Silica-decorated magnetic nanocomposites for catalytic applications, *Coord. Chem. Rev.*, 2015, **288**, 118–143.

4 D. K. Yi, S. S. Lee and J. Y. Ying, Synthesis and applications of magnetic nanocomposite catalysts, *Chem. Mater.*, 2006, **18**, 2459–2461.

5 K. Kan-Dapaah, N. Rahbar, A. Tahlil, D. Crosson, N. Yao and W. Soboyejo, Mechanical and hyperthermic properties of magnetic nanocomposites for biomedical applications, *J. Mech. Behav. Biomed. Mater.*, 2015, **49**, 118–128.

6 S. Kalia, S. Kango, A. Kumar, Y. Haldorai and R. Kumar, Magnetic polymer nanocomposites for environmental and biomedical applications, *Colloid Polym. Sci.*, 2014, **292**, 2025–2052.

7 S. H. Hussein-Al-Ali, M. E. El Zowalaty, M. Z. Hussein, M. Ismail, D. Dorniani and T. J. Webster, Novel kojic acid-polymer-based magnetic nanocomposites for medical applications, *Int. J. Nanomed.*, 2014, **9**, 351–362.

8 B. H. McDonagh, G. Singh, S. Hak, S. Bandyopadhyay, I. L. Augestad, D. Peddis, I. Sandvig, A. Sandvig and W. R. Glomm, L-DOPA-coated manganese oxide nanoparticles as dual MRI contrast agents and drug-delivery vehicles, *Small*, 2016, **12**, 301–306.

9 Y. Li, T. Jing, G. Xu, J. Tian, M. Dong, Q. Shao, B. Wang, Z. Wang, Y. Zheng, C. Yang and Z. Guo, 3-D magnetic graphene oxide-magnetite poly(vinyl alcohol) nanocomposite substrates for immobilizing enzyme, *Polymer*, 2018, **149**, 13–22.

10 K. Gong, Q. Hu, L. Yao, M. Li, D. Sun, Q. Shao, B. Qiu and Z. Guo, Ultrasonic pretreated sludge derived stable magnetic active carbon for Cr(VI) removal from wastewater, *ACS Sustainable Chem. Eng.*, 2018, **6**, 7283–7291.

11 J. Huang, Y. Cao, Q. Shai, X. Peng and Z. Guo, Magnetic nanocarbon adsorbents with enhanced hexavalent chromium removal: morphology dependence of fibrillar vs particulate structures, *Ind. Eng. Chem. Res.*, 2017, **56**, 10689–10701.

12 J. Huang, Y. Li, Y. Cao, F. Peng, Y. Cao, Q. Shao, H. Liu and Z. Guo, Hexavalent chromium removal over magnetic carbon nanoadsorbents: synergistic effect of fluorine and nitrogen co-doping, *J. Mater. Chem. A*, 2018, **6**, 13062–13074.

13 N. Wu, C. Liu, D. Xu, J. Liu, W. Liu, Q. Shao and Z. Guo, Enhanced electromagnetic wave absorption of three-dimensional porous Fe_3O_4/C composite flowers, *ACS Sustainable Chem. Eng.*, 2018, **6**, 12471–12480.

14 J. Guo, H. Song, H. Liu, C. Luo, Y. Ren, T. Ding, M. A. Khan, D. P. Young, X. Liu, X. Zhang, J. Kong and Z. Guo, *J. Mater. Chem. C*, 2018, **5**, 5334–5344.

15 P. Xie, H. Li, B. He, F. Dang, J. Lin, R. Fan, C. Hou, H. Liu, J. Zhang, Y. Ma and Z. Guo, *J. Mater. Chem. C*, 2018, **6**, 8812–8822.

16 C. Wang, V. Murugadoss, J. Kong, Z. He, X. Mai, Q. Shao, Y. Chen, L. Guo, C. Liu, S. Angaiah and Z. Guo, *Carbon*, 2018, **140**, 696–733.

17 Q. Luo, H. Chen, Y. Lin, H. Du, Q. Hou, F. Hao, N. Wang, Z. Guo and J. Huang, Discrete iron(III) oxide nanoislands for efficient and photostable perovskite solar cells, *Adv. Funct. Mater.*, 2017, **27**, 1702090.

18 Y. He, S. Yang, H. Liu, Q. Shao, Q. Chen, C. Lu, Y. Jiang, C. Liu and Z. Guo, Reinforced carbon fiber laminates with oriented carbon nanotube epoxy nanocomposites: magnetic field assisted alignment and cryogenic temperature mechanical properties, *J. Colloid Interface Sci.*, 2018, **517**, 40–51.

19 J. Zhao, L. Wu, C. Zhan, Q. Shao, Z. Guo and L. Zhang, Overview of polymer nanocomposites: computer simulation understanding of physical properties, *Polymer*, 2017, **133**, 272–287.

20 H. Gu, H. Zhang, J. Lin, Q. Shao, D. P. Young, L. Sun, T. D. Shen and Z. Guo, Large negative giant magnetoresistance at room temperature and electrical transport in cobalt ferrite-polyaniline nanocomposites, *Polymer*, 2018, **143**, 324–330.

21 E. Dagotto, Complexity in strongly correlated electronic systems, *Science*, 2005, **309**, 257–262.

22 B. Keimer, S. A. Kivelson, M. R. Norman, S. Uchida and J. Zaanen, From quantum matter to high-temperature superconductivity in copper oxides, *Nature*, 2015, **518**, 179–186.

23 H. S. Lee, S. G. Choi, H.-H. Park and M. J. Rozenberg, A new route to the Mott-Hubbard metal-insulator transition: strong correlations effects in $Pr_{0.7}Ca_{0.3}MnO_3$, *Sci. Rep.*, 2013, **3**, 1704.

24 T. Taniguchi, H. Kadowaki, H. Takatsu, B. Fåk, J. Ollivier, T. Yamazaki, T. J. Sato, H. Yoshizawa, Y. Shimura, T. Sakakibara, T. Hong, K. Goto, L. R. Yaraskavitch and J. B. Kycia, Long-range order and spin-liquid states of polycrystalline $Tb_{2+x}Ti_{2-x}O_{7+y}$, *Phys. Rev. B: Condens. Matter Mater. Phys.*, 2015, **87**, 060408(R).

25 Y. Tokura and Y. Tomioka, Colossal magnetoresistive manganites, *J. Magn. Magn. Mater.*, 1999, **200**, 1–23.

26 Y. Tokura, S. Seki and N. Nagaosa, Multiferroics of spin origin, *Rep. Prog. Phys.*, 2014, **77**, 076501.

27 T. Sarkar, B. Ghosh and A. K. Raychaudhuri, Crystal structure and physical properties of half-doped manganite nanocrystals of less than 100-nm size, *Phys. Rev. B: Condens. Matter Mater. Phys.*, 2008, **77**, 235112.

28 T. Sarkar, A. K. Raychaudhuri and T. Chatterji, Size induced arrest of the room temperature crystallographic structure in nanoparticles of $La_{0.5}Ca_{0.5}MnO_3$, *Appl. Phys. Lett.*, 2008, **92**, 123104.

29 T. Sarkar, A. K. Raychaudhuri, A. K. Bera and S. M. Yusuf, Effect of size reduction on the ferromagnetism of the manganite $La_{1-x}Ca_xMnO_3$ (x=0.33), *New J. Phys.*, 2010, **12**, 123026.

30 T. Sarkar, M. V. Kamalakar and A. K. Raychaudhuri, Electrical transport properties of nanostructured ferromagnetic perovskite oxides $La_{0.67}Ca_{0.33}MnO_3$ and $La_{0.5}Sr_{0.5}CoO_3$ at low temperatures (5 K ≥ T ≥ 0.3 K) and high magnetic field, *New J. Phys.*, 2012, **14**, 033026.

31 D. Lahiri, S. Khalid, T. Sarkar, A. K. Raychaudhuri and S. M. Sharma, XAFS investigation of the role of orientational disorder in the stabilization of the ferromagnetic metallic phase in nanoparticles of $La_{0.5}Ca_{0.5}MnO_3$, *J. Phys.: Condens. Matter*, 2012, **24**, 336001.

32 L. Pagliari, M. Dapiaggi, F. Maglia, T. Sarkar, A. K. Raychaudhuri, T. Chatterji and M. A. Carpenter, Strain heterogeneity and magnetoelastic behaviour of nanocrystalline half-doped La, Ca manganite, $La_{0.5}Ca_{0.5}MnO_3$, *J. Phys.: Condens. Matter*, 2014, **26**, 435303.

33 G. Muscas, P. A. Kumar, G. Barucca, G. Concas, G. Varvaro, R. Mathieu and D. Peddis, Designing new ferrite/manganite nanocomposites, *Nanoscale*, 2016, **8**, 2081–2089.

34 S. A. Ivanov, R. Tellgren, F. Porcher, T. Ericsson, A. Mosunov, P. Beran, S. K. Korchagina, P. Anil Kumar, R. Mathieu and P. Nordblad, Preparation, structural, dielectric and magnetic properties of $LaFeO_3$-$PbTiO_3$ solid solutions, *Mater. Res. Bull.*, 2012, **47**, 3253–3268.

35 J. Lu, A. Günther, F. Schrettle, F. Mayr, S. Krohns, P. Lunkenheimer, A. Pimenov, V. D. Travkin, A. A. Mukhin and A. Loidl, On the room temperature multiferroic $BiFeO_3$: magnetic, dielectric and thermal properties, *Eur. Phys. J. B*, 2010, **75**, 451–460.

36 H. Zheng, J. Wang, S. E. Lofland, Z. Ma, L. Mohadder-Ardabili, T. Zhao, L. Salamanca-Riba, S. R. Shinde, S. B. Ogale, F. Bai, D. Viehland, Y. Jia, D. G. Schlom, M. Wuttig, A. Roytburd and R. Ramesh, Multiferroic $BaTiO_3$-$CoFe_2O_4$ Nanostructures, *Science*, 2004, **303**, 661–663.

37 H. Lv, X. Liang, Y. Cheng, H. Zhang, D. Tang, B. Zhang, G. Ji and Y. Du, Coin-like α-Fe_2O_3@$CoFe_2O_4$ core-shell composites with excellent electromagnetic absorption performance, *ACS Appl. Mater. Interfaces*, 2015, **7**, 4744–4750.

38 W. Liu, J. Liu, Z. Yang and G. Ji, Extended working frequency of ferrites by synergistic attenuation through a controllable carbothermal route based on Prussian blue shell, *ACS Appl. Mater. Interfaces*, 2018, **10**, 28887–28897.

39 H. Lv, H. Zhang, B. Zhang, G. Ji, Y. He and Q. Lin, A proposed electron transmission mechanism between Fe^{3+}/Co^{2+} and Fe^{3+}/Fe^{3+} in the spinel structure and its practical evidence in quaternary $Fe_{0.5}Ni_{0.5}Co_2S_4$, *J. Mater. Chem. C*, 2016, **4**, 5476–5482.

40 X. Zhang, G. Ji, W. Liu, B. Quan, X. Linag, C. Shang, Y. Cheng and Y. Du, Thermal conversion of an Fe3O4@metal-organic framework: a new method for an

efficient Fe-Co/nanoporous carbon microwave absorbing material, *Nanoscale*, 2015, **7**, 12932–12942.

41 N. M. Aimon, H. K. Choi, X. Y. Sun, D. H. Kim and C. A. Ross, Templated self-assembly of functional oxide nanocomposites, *Adv. Mater.*, 2014, **26**, 3063–3067.

42 C. Cannas, A. Falqui, A. Musinu, D. Peddis and G. Piccaluga, $CoFe_2O_4$ nanocrystalline powders prepared by citrate-gel methods: synthesis, structure and magnetic properties, *J. Nanopart. Res.*, 2006, **8**, 255–267.

43 C. Cannas, A. Musinu, D. Peddis and G. Piccaluga, New synthesis of ferrite–silica nanocomposites by a sol–gel auto-combustion, *J. Nanopart. Res.*, 2004, **6**, 223–232.

44 G. K. Williamson and W. H. Hall, X-ray line broadening from filed aluminium and wolfram, *Acta Metall.*, 1953, **1**, 22–31.

45 D. Peddis, F. Orrù, A. Ardu, C. Cannas, A. Musinu and G. Piccaluga, Interparticle Interactions and Magnetic Anisotropy in Cobalt Ferrite Nanoparticles: Influence of Molecular Coating, *Chem. Mater.*, 2012, **24**, 1062–1071.

46 Z. Sun, L. Zhang, F. Dang, Y. Liu, Z. Fei, Q. Shao, H. Lin, J. Guo, L. Xiang, N. Yerra and Z. Guo, Experimental and simulation-based understanding of morphology controlled barium titanate nanoparticles under co-adsorption of surfactants, *CrystEngComm*, 2017, **19**, 3288–3298.

47 T. Liu, K. Yu, L. Gao, H. Chen, N. Wang, L. Hao, T. Li, H. He and Z. Guo, A graphene quantum dot decorated SrRuO3 mesoporous film as an efficient counter electrode for high-performance dye-sensitized solar cells, *J. Mater. Chem. A*, 2017, **5**, 17848–17855.

48 L. Zhang, W. Yu, C. Han, J. Guo, Q. Zhang, H. Xie, Q. Shao, Z. Sun and Z. Guo, Large scaled synthesis of heterostructured electrospun TiO_2/SnO_2 nanofibers with an enhanced photocatalytic activity, *J. Electrochem. Soc.*, 2017, **164**, H651–H656.

49 L. Zhang, M. Qin, W. Yu, Q. Zhang, H. Xie, Z. Sun, Q. Shao, X. Guo, L. Hao, Y. Zheng and Z. Guo, Heterostructured TiO_2/WO_3 nanocomposites for photocatalytic degradation of toluene under visible light, *J. Electrochem. Soc.*, 2017, **164**, H1086–H1090.

50 B. Song, T. Wang, H. Sun, Q. Shao, J. Zhao, K. Song, L. Hao, L. Wang and Z. Guo, Two-step hydrothermally synthesized carbon nanodots/WO_3 photocatalysts with enhanced photocatalytic performance, *Dalton Trans.*, 2017, **46**, 15769–15777.

51 Y. Zheng, Y. Zheng, S. Yang, Z. Guo, T. Zhang, H. Song and Q. Shao, Esterification synthesis of ethyl oleate catalyzed by Bronsted acid-surfactant-combined ionic liquid, *Green Chem. Lett. Rev.*, 2017, **10**, 202–209.

52 Y. Zheng, Y. Zheng, Z. Wang, Y. Cao, Q. Shao and Z. Guo, Sodium dodecyl benzene sulfonate-catalyzed reaction for aromatic aldehydes with 1-phenyl-3-methyl-5-pyrazolone in aqueous media, *Green Chem. Lett. Rev.*, 2018, **11**, 217–223.

53 T.-J. Park, G. C. Papaefthymiou, A. J. Viescas, A. R. Moodenbaugh and S. S. Wong, Size-dependent magnetic properties of single-crystalline multiferroic $BiFeO_3$ nanoparticles, *Nano Lett.*, 2007, **7**, 766–772.

54 C. Liu, X. Wu, T. Klemmer, N. Shukla and D. Weller, Reduction of sintering during annealing of FePt nanoparticles coated with iron oxide, *Chem. Mater.*, 2005, **17**, 620–625.

55 A. López-Ortega, M. Estrader, G. Salazar-Alvarez, A. G. Roca and J. Nogués, Applications of exchange coupled bi-magnetic hard/soft and soft/hard magnetic core/shell nanoparticles, *Phys. Rep.*, 2015, **553**, 1–32.

56 D. Peddis, P. E. Jönsson, S. Laureti and G. Varvaro, Magnetic interactions: A tool to modify the magnetic properties of materials based on nanoparticles, *Front. Nanosci.*, 2014, **6**, 129–188.